IPEM | Institute of Physics and Engineering in Medicine

Calculation of positron range and its effect on the fundamental limit of positron emission tomography system spatial resolution

To cite this article: Craig S Levin and Edward J Hoffman 1999 *Phys. Med. Biol.* **44** 781
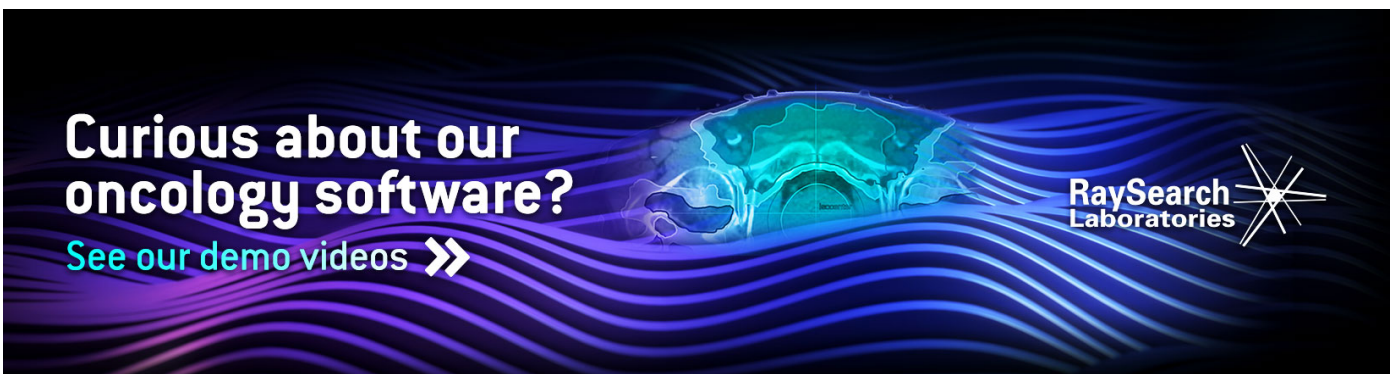
View the article online for updates and enhancements.

Related content

- Study of PET intrinsic spatial resolution and contrast recovery improvement for PET/MRI systems
  Hao Peng and Craig S Levin

- MicroPET II: design, development and initial performance of an improved microPET scanner for small-animal imaging
  Yuan-Chuan Tai, Arion F Chatziioannou, Yongfeng Yang et al.

- Positron range estimations with PeneloPET
  J Cal-González, J L Herraiz, S España et al.

Recent citations

- Impact of the Noise Penalty Factor on Quantification in Bayesian Penalized Likelihood (Q.Clear) Reconstructions of 68Ga-PSMA PET/CT Scans
  Sjoerd Rijnsdorp *et al*

- Evolution of PET Detectors and Event Positioning Algorithms Using Monolithic Scintillation Crystals
  Andrea Gonzalez-Montoro *et al*

- H2RSPET: a 0.5 mm resolution high-sensitivity small-animal PET scanner, a simulation study
  Youfang Lai *et al*

Calculation of positron range and its effect on the fundamental limit of positron emission tomography system spatial resolution

Craig S Levin†‡ and Edward J Hoffman†

† UCLA School of Medicine, Laboratory of Nuclear Medicine, Los Angeles, CA 90095, USA
‡ UCSD School of Medicine, Department of Radiology and VA Medical Center, Nuclear Medicine Division, San Diego, CA 92161, USA

Abstract. Developments in positron emission tomography (PET) technology have resulted in systems with finer detector elements designed to further improve spatial resolution. However, there is a limit to what extent reducing detector element size will improve spatial resolution in PET. The spatial resolution of PET imaging is limited by several other factors, such as annihilation photon non-collinearity, positron range, off-axis detector penetration, detector Compton scatter, undersampling of the signal in the linear or angular directions for the image reconstruction process, and patient motion. The overall spatial resolution of the systems is a convolution of these components. Of these other factors that contribute to resolution broadening, perhaps the most uncertain, poorly understood, and, for certain isotopes, the most dominant effect is from positron range. To study this latter effect we have developed a Monte Carlo simulation code that models positron trajectories and calculates the distribution of the end point coordinates in water for the most common PET isotopes used: ^{18}F, ^{13}N, ^{11}C and ^{15}O. In this work we present some results from these positron trajectory studies and calculate what effect positron range has on the overall PET system spatial resolution, and how this influences the choice of PET system design parameters such as detector element size and system diameter. We found that the fundamental PET system spatial resolution limit set from detector size, photon non-collinearity and positron range alone varied from nearly 1 mm FWHM (2 mm FWTM) for a 10–20 cm diameter system typical for animal studies with ^{18}F to roughly 4 mm FWHM (7 mm FWTM) for an 80 cm diameter system typical for human imaging using ^{15}O.

1. Introduction

The recent interest in the development of high-resolution PET scanners for animal imaging (Cherry *et al* 1996, Schmelz *et al* 1995, Seidel *et al* 1994, Watanabe *et al* 1995, Weber *et al* 1995) motivates the question: what is the ultimate system spatial resolution that can be achieved? The spatial resolution of PET imaging is limited by several factors such as detector size, annihilation photon non-collinearity, positron range of the isotope of interest, off-axis detector penetration, detector Compton scatter, undersampling of the signal in the linear or angular directions for the image reconstruction process, and patient motion. Because the overall resolution is a convolution of these components, when designing a high-resolution PET imaging system it is important to understand that reducing detector element size alone will produce only limited improvements in the resulting system spatial resolution.

Of the components that contribute to resolution broadening, perhaps the most uncertain, poorly understood, and, for certain isotopes and scanners, most dominant effect is from positron range. Early experimental efforts (Phelps *et al* 1975, Cho *et al* 1975, Hoffman *et al* 1976) to measure the distribution of annihilation points for medically important positron emitters in water were of limited accuracy since the detector resolution was comparable to the 'positron range' effect of interest. Derenzo (1979) estimated this component by measuring annihilation point spread distributions (a.k.a. 'positron range blurring functions') in low-density polyurethane foam, where the annihilation point distributions are significantly expanded, and in aluminium, where effects other than positron range dominate spatial broadening. The deconvolved positron range distribution data were then fitted to an empirical function, and the results were scaled by density to the water equivalent values using range-energy relation data for electrons (Katz and Penfold 1952).

There are a few potential difficulties inherent to Derenzo's approach:

(a) Because the attenuation of electrons and positrons (betas) in a medium is a complicated function of the density and effective atomic number, among other parameters, it is difficult to extrapolate measured range results from polyurethane to water by simple scaling with density.

(b) To determine the contribution of positron 'range' to the spatial resolution in PET, it is the spatial extent of the annihilation point distribution that is important, rather than the range or maximum extent which the range-energy relation data of Katz and Penfold (1952) represent.

(c) The deconvolution process used to obtain the annihilation point distribution will result in some loss of information inherent in the reported data.

(d) Effects such as Compton scatter and detector width can cause positioning errors in the distribution measurement.

(e) It would be challenging to apply this method to the measurement of range distributions from short-lived isotopes such as ^{13}N and ^{15}O.

Later, Palmer and Brownell (1992) evaluated the annihilation density distribution for certain positron emitters through calculations based on a model which employs beta-decay energy spectra combined with an empirical range formula, assuming that positrons behave diffusively. Recently, Monte Carlo simulation studies of positron trajectories in water were performed (Iida *et al* 1986, Raylman *et al* 1996, Rickey *et al* 1991, Wirrwar *et al* 1997) with the goal of evaluating potential PET spatial resolution improvements due to the presence of high magnetic fields.

Our goal in this work is to develop a general model using the Monte Carlo method based on the interactions that the positron undergoes when traversing a dense medium. For the calculation of positron annihilation point distribution, the Monte Carlo approach has the potential for high accuracy provided that the modelling performed incorporates sufficient detail. This code (Levin *et al* 1997) will allow us to calculate any annihilation point distribution in terms of only physical parameters of the positron emitter and the absorbing medium without the use of empirical formulae and systematic assumptions. We then make estimates of the fundamental limits on PET system spatial resolution expected with ^{18}F, ^{13}N, ^{11}C and ^{15}O isotopes for various system design parameters such as detector element size and diameter. Standard Monte Carlo code packages exist such as GEANT (CERN, Geneva, Switzerland), ITS (Sandia National Laboratories, Albuquerque, NM) and EGS (SLAC, Palo Alto, CA) that are capable of calculating positron end point coordinate fluctuations. The main disadvantage of these packages, besides their size and complexity, are that they were originally developed to study higher-energy radiation processes, and may not be sufficiently accurate in calculating charged particle trajectories involving energies less than 300 keV.

2. Materials and methods

2.1. Effects included in the positron trajectory calculation

For beta particle energies in the range 10^4–10^7 eV, their deflection in matter is due almost entirely to the elastic collisions with the atomic nuclei, while the energy loss, except that due to bremsstrahlung, which is practically negligible for the positron energy ranges of interest, results from the interaction with the atomic electrons. Therefore, it is possible to treat the two phenomena separately, though of course they always occur together. It is also important to note that for the energy range of interest in this work there is an insignificant difference between the energy loss and multiple scattering of positrons and electrons (Rohrlich and Carlson 1954).

2.1.1. Multiple Coulomb elastic scattering from the nucleus: Moliere's theory.

In the following development we have closely followed Bethe's treatment of Moliere's theory of multiple Coulomb scattering (Bethe 1953). This theory described the scattering of fast charged particles in a screened Coulomb field. Some of the same expressions and parametrizations used in that article will be presented in this work and incorporated into the Monte Carlo calculation.

The probability that an electron of momentum p and velocity v is scattered into the angle θ and angular interval $d\theta$ after traversing a thickness t in a material of atomic number Z and density of atoms N is given by

$$f(\theta)\theta \, d\theta = \lambda \, d\lambda \int_0^\infty y \, dy \, J_0(\lambda y) \exp[\tfrac{1}{4}y^2(-b + \ln \tfrac{1}{4}y^2)] \tag{1}$$

where y is a dummy variable, $\lambda = \theta/\chi_c$, and b is defined by

$$e^b = \frac{\chi_c^2}{1.167\chi_a^2}. \tag{2}$$

χ_c is the angle parameter and characterizes the minimum single scattering angle that can occur:

$$\chi_c^2 = \frac{4\pi N t e^4 Z(Z+1)}{(pv)^2}. \tag{3}$$

χ_a is the characteristic screening angle and is given in Moliere's approximation as

$$\chi_a^2 = \chi_0^2(1.13 + 3.76\alpha^2). \tag{4}$$

χ_0 is the critical angle below which deviations from the Rutherford scattering law (with the characteristic $1/\theta^4$ form) become apparent because of nuclear effects. It is given by

$$\chi_0 = \frac{\lambda'}{0.885a_0 Z^{-1/3}}. \tag{5}$$

α is the fine structure constant, λ' is the electron DeBroglie wavelength and a_0 is the Bohr radius.

In the derivation of $f(\theta)$ Bethe assumed $\chi_0 \ll \chi_c$, which is true for reasonably thick t, but will fail for y of the order of $\chi_c/\chi_0 \sim e^{b/2}$. The quantity $e^b \sim (\chi_c/\chi_a)^2$ is approximately the number of collisions Ω_0 that occur in the thickness t of water atoms. By examining the above formulae we see that, for example, in a low-pressure gas, Moliere's theory of small-angle multiple scatter breaks down. Moliere considered his model to be valid for $\Omega_0 > 20$ and when the parameter B (defined below) >4.5. In this work we found that in water at room temperature, an 80 keV beta that travels a maximum range of 0.14 mm, has $\Omega_0 \approx 30$ and $B \approx 5$; so we expect Moliere's theory to apply. However, a 50 keV beta with a maximum range of 0.06 mm in water has $\Omega_0 \approx 20$, which is near the region where Moliere's theory

breaks down. So we expect there to be a discrepancy between theory and measurement below 50 keV.

Moliere evaluated $f(\theta)$ for all angles by a change of variable $\vartheta = \theta/(\chi_c B^{1/2})$. B is a constant defined by $b = B - \ln B$. With these definitions $f(\vartheta)$ can be expanded in a power series in B^{-1}:

$$f(\theta)\theta\,\mathrm{d}\theta = \vartheta\,\mathrm{d}\vartheta(f^{(0)}(\vartheta) + B^{-1}f^{(1)}(\vartheta) + B^{-2}f^{(2)}(\vartheta) + \cdots) \tag{6}$$

where

$$f^{(n)}(\vartheta) = \frac{1}{n!}\int_0^\infty u\,\mathrm{d}u\,J_0(\vartheta u)\exp\left(-\frac{u^2}{4}\right)\left[\frac{u^2}{4}\ln\left(\frac{u^2}{4}\right)\right]^n \tag{7}$$

with $u = B^{1/2}y$. In the limit of large angles, the distribution function tends toward the Rutherford single scattering law: $f_R(\theta)\theta\,\mathrm{d}\theta = (2/B)\,\mathrm{d}\vartheta/\vartheta^3$. The ratio of Moliere to Rutherford scattering probabilities is $R = f/f_R = 1/2\vartheta^4(f^{(1)} + B^{-1}f^{(2)} + \cdots)$, which gives asymptotic expressions for f^1 and f^2. Together with $f^{(0)}$ obtained from $f^{(n)}$ above we have

$$f^{(0)}(\vartheta) = 2\,\mathrm{e}^{-\vartheta}$$
$$f^{(1)}(\vartheta) = \frac{2(1 - 5\vartheta^{-2})^{-4/5}}{\vartheta^4} \tag{8}$$
$$f^{(2)}(\vartheta) = \frac{16(\ln\vartheta + \ln 0.4)}{\vartheta^6(1 - 9\,\vartheta^{-2} - 24\,\vartheta^{-4})}.$$

For $\vartheta > 4$ (large θ) these expressions will be used in our simulation. For $\vartheta < 4$ (small θ) we will use the values in table II of Bethe's paper (Bethe 1953) to determine $f^{(1)}$ and $f^{(2)}$.

In the simulation we will not use approximations to $f(\theta)$ for small and large values of θ since it is not a simple function for the entire angular range of interest. We will use rejection techniques for generating $f(\theta)$. If x and y are random numbers (both between 0 and 1), the standard method is to generate $f(x)$ and accept x provided $f(x)/f(0) < y$. However, since $f(x)$ rapidly decreases with x, this method is inefficient. A better approach is to first generate x in a trial function $e(x) > f(x)/f(0)$. We accept x provided $ye(x) > f(x)/f(0)$. The most appealing choice for $e(x)$ is a Gaussian. Note that although this technique of choosing the distribution $e(x)$ improves the efficiency of generating $f(x)$ there will be a smaller range of values of x that will be accepted. Any error in the generation of $f(\theta)$ would probably be due to not using enough terms in the expansion.

2.1.2. Energy loss through inelastic collisions: excitation and ionization. Betas traversing matter lose their energy through inelastic collisions with the atomic electrons, by which the atoms are excited and ionized. Energy loss due to the emission of bremsstrahlung in the Coulomb field of the nucleus will be ignored here due to the low probability of occurrence for the positron energy range of interest (Siegbahn 1955).

The interaction of the incident betas with the atomic electrons in matter is characterized by the fact that the energy transferred to the atoms per collision is very small. Even for very high primary energies, excitation is more probable than ionization, and the resulting secondary electrons have a mean kinetic energy of only a few eV. The total energy loss after passage through a given thickness of matter is therefore the result of a very large number of small energy losses. The average energy lost per distance traversed by an ionizing particle in a material made of independent atoms and due to only inelastic processes (ionization and excitation) is given by the Bethe–Bloch formula (Knoll 1989, Leo 1987):

$$\frac{\mathrm{d}E}{\mathrm{d}x} = 4\pi r_0^2\frac{mc^2}{\beta^2}NZ(A + B) \tag{9}$$

with

$$A = \ln\left(\frac{\beta\gamma\sqrt{\gamma-1}mc^2}{I}\right)$$

and

$$B = \frac{1}{2\gamma^2}\left(\frac{(\gamma-1)^2}{8} + 1 - (2\gamma^2 + 2\gamma - 1)\ln 2\right) \tag{10}$$

where r_0 is the classical electron radius, $\gamma = (1-\beta)^{-1/2}$, N the number density of atoms for the medium (water), Z the atomic number and I the average excitation potential of the medium in eV (which for $Z_{\text{eff}} < 13$ is approximately (Leo 1987) $I = 12Z + 7 = 94$ eV for water, using $Z_{\text{eff}} = 7.22$). By studying the above formulae we see the value for dE/dx rapidly increases as the electron slows down and therefore most of the ionization created in an electron track will be towards the end. We also see that there is a nonlinear relationship between energy and range for non-relativistic charged particles (betas with energy less than 200 keV) and due to an energy spectrum peaked toward lower energies, a significant fraction of emitted positrons travel less than 0.5 mm.

2.1.3. Hard elastic collisions: delta or 'knock-on' electrons'. Relatively hard electron–electron collisions often cause the emission of energetic secondary electrons, commonly called delta electrons. These delta electrons have the capability of producing further ionization. The number of these secondary electrons of energy E_δ emitted per unit distance and created by an incident beta of kinetic energy T_1, in a medium with electron density N_e, is given by (Ritson 1961)

$$N_\delta(E_\delta, T_1) = \frac{W(T_1)}{E_\delta^2} \tag{11}$$

where

$$W(T_1) = \frac{2\pi r_0^2 m_e N_e}{\beta^2} \tag{12}$$

in the units in which h (Planck's constant) $= c$ (speed of light) $= 1$. This formula is valid for $E_\delta \ll T_1$. However, since it is derived for relatively hard collisions we will impose a lower energy cut-off of 50 keV, below which delta electrons are not produced. The decision of whether or not a delta electron is ejected is made using rejection techniques based on the above formulae. If a delta electron is produced, the energy of the incident electron becomes $T_1 - E_\delta$. The energy, momentum and location of a delta electron produced are stored for treatment in later iterations in the trajectory simulation, where the new particle is treated as the incident particle. Delta electrons are typically more energetic than those that result from ordinary inelastic collisions and may be ejected at large angles with respect to the positron's track. Thus, including delta electron production has the effect of, on average, increasing the transverse dimension and decreasing the longitudinal dimension of a given positron's trajectory through matter relative to its direction of entry.

2.1.4. Energy spectra. In order to calculate the positron trajectories for a given isotope, the correct energy spectra must be known. The end point energies of the ^{18}F, ^{11}C, ^{13}N and ^{15}O positron spectra are 635, 970, 1190 and 1720 keV respectively (with corresponding mean energies of 250, 390, 490 and 740 keV, and half-lives of 110, 20.4, 9.96, and 2.07 min). Fortunately, these isotopes are all *allowed* or *super-allowed* beta decays and the energy spectra

have known analytical expressions (Wu and Moskowski 1966, Daniel 1968) which can easily be calculated. The theoretical energy distribution is of the form

$$N(E)\, \mathrm{d}E = g F(Z, E) p E (E_{\max} - E)^2\, \mathrm{d}E \tag{13}$$

where $N(E)$ is the number of decays at energy E, g is a coupling constant, E is the total β energy in units of mc^2, $E_{\max}$ is the maximum (end point) energy of the β particle in units of mc^2, p is the momentum of β in units of mc, $F(Z, E)$ is the Fermi function, and Z is the atomic number of the beta decay daughter. The Fermi function takes into account the Coulomb interaction between the beta and the daughter nucleus. A non-relativistic approximation for $F(Z, E)$, valid for *allowed* transitions of lighter elements (Wu and Moskowski 1966, Daniel 1968) is

$$F_{\text{allowed}}(Z, E) = 2\pi\eta/(1 - \mathrm{e}^{-2\pi\eta}) \tag{14}$$

with $\eta = -Z\alpha E/p$ for positron decay, and $\alpha = 1/137$, the fine structure constant. The theoretical energy spectra for the four isotopes of interest are shown in figure 1.
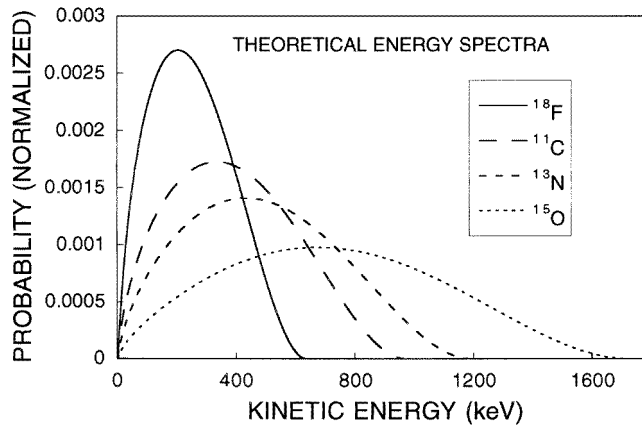
Figure 1. Theoretical positron kinetic energy spectra for ^{18}F, ^{11}C, ^{13}N and ^{15}O (normalized to have equal area under the curves).
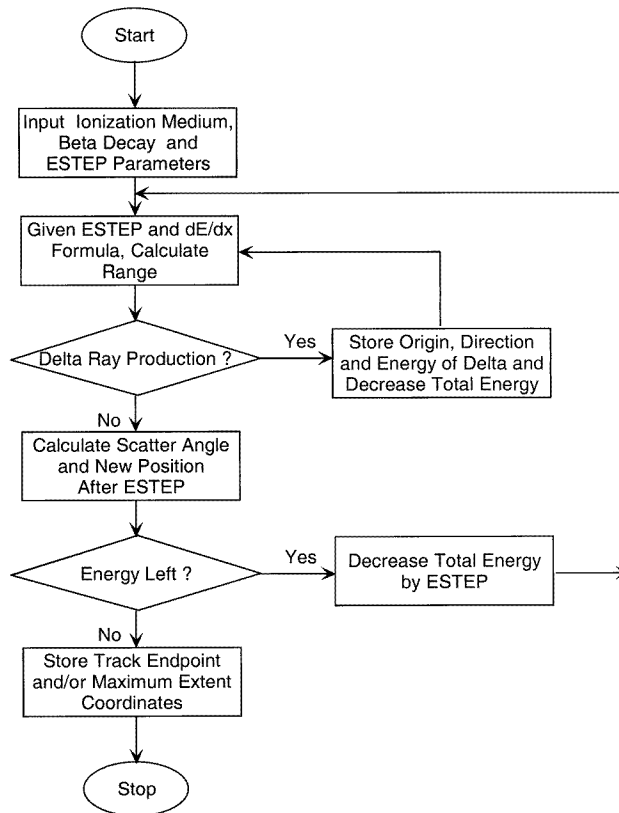
2.2. The Monte Carlo calculation

The trajectory of a positron in water is best followed in terms of small track segments beginning at the origin of the decay. The most obvious procedure is to allow the positron to traverse a given thickness and then determine the energy lost after completing that step. However, due to large values of $\mathrm{d}E/\mathrm{d}x$ toward the end of a trajectory, the distance traversed for a given energy step rapidly decreases in that region, especially for high-density media. Since this 'step' will be used as the target thickness in the multiple scatter calculation, the assumption $\chi_c \gg \chi_a$ (or >20 collisions) and, thus, the multiple scatter formulation could break down towards the end region of a given trajectory.

Instead, we chose to generate the positron track by degrading the initial energy E_0 in small, fixed steps ESTEP $\ll E_0$, and calculate the range R (in three dimensions) that the electron must travel in order to lose ESTEP to inelastic collisions (ionization and excitation). This R is used as the 'track segment' and target thickness in the multiple scatter formulae. The energy step size used was approximately 3 keV. We then check to see if any energy degradation processes other than excitation and ionization have occurred (delta electron production) as the particle completes this step. If so, the initial energy is degraded accordingly, as described in

section 2.1.3. The number of delta electrons created from a given incident positron, as well as their locations, energies and momenta, are stored in various arrays and will be used in later iterations that treat each of these new electrons as the 'primary' particle.

We then evaluate χ_c and B in the multiple scattering calculation using R as the target thickness in the formulae. The direction θ that the positron scatters into due to multiple scattering is generated using $f(\theta)$ as discussed in section 2.1.1, and the azimuth angle ϕ is randomly generated between 0 and 2π. At the completion of this step, the positron coordinate frame, in which θ and ϕ are determined, must be rotated back to the fixed laboratory coordinate system. The transformed angles together with R are then used to calculate the new x, y and z coordinates of the particle. That is, given R, θ and ϕ, we find the new location of the positron after the given energy loss and length traversed in spherical coordinates. Starting from this new position the next segment is treated in the same manner using the new energy E_0-ESTEP. This entire process continues until the energies of the primary and all of the energetic secondary electrons produced are reduced to zero or until χ_c/χ_a reaches a given value below which the multiple scattering calculation is no longer valid.

Figure 2. Flow chart for the Monte Carlo simulation to calculate beta trajectories.

The flow-chart for this entire algorithm, written in FORTRAN, is shown in figure 2. For the positron annihilation point distribution calculation the end point of the positron's track is found for each event simulated. We assumed point sources of ^{18}F, ^{11}C, ^{13}N and ^{15}O positrons. To simulate 10 000 events (positron tracks) takes approximately 20 s on a VAX 4000.

2.3. Experimental validation

For the experimental validation of the trajectory simulation, electron absorption measurements were performed using a ^{204}Tl source ($E_{max} = 765$ keV), thin (125 μm) plastic sheets, and a 2.5 cm diameter, 1.5 mm thick CaF$_2$(Eu) scintillation crystal coupled to a 7.5 cm diameter photomultiplier tube. The advantages of using a ^{204}Tl electron source and plastic absorber for the experimental validation are its simplicity compared to obtaining a positron point source in water, its long half-life (3.8 years), and the absence of annihilation background (and associated positioning errors due to Compton scatter and detector size). In principle, for the energy range of interest, effects such as multiple scattering, ionization, excitation and the production of delta electrons are independent of the magnitude of the charge of the beta particle, and only the general shape of the input theoretical beta spectrum changes. With the ^{204}Tl source at a fixed 10 cm distance above the detector, the plastic sheets were sequentially stacked upon the detector, and the transmitted energy spectrum in the CaF$_2$(Eu) was measured (for a fixed acquisition time) versus the total thickness of plastic absorber. The maximum range of ^{204}Tl betas in CaF$_2$(Eu) is roughly 0.6 mm (Levin *et al* 1996) so that all electrons hitting the crystal are stopped. Any background, non-beta-emitting 'source' effects, such as from emitted x-rays from the aluminium source backing, were estimated and subtracted from the measured spectra by acquiring a spectrum with the crystal shielded by a 6 mm thick plastic absorber intended to shield only the betas. The results of these studies were compared with those results obtained by simulating the corresponding experimental conditions with the Monte Carlo beta trajectory code (Z_{eff}(plastic) $= 6.7$, $\rho = 1.1$ g cm^{-3}, similar to the corresponding values for water). For beta absorption studies, the maximum extent is relevant rather than the end point coordinate because the beta is likely to scatter backwards towards the end of its track. This is due to the fact that the multiple scatter angle is inversely related to the beta particle energy, and where the energy is lowest, the scatter angle is the highest.

2.4. System spatial resolution factors in positron emission tomography

The spatial resolution is a three-dimensional parameter. It is common in PET to represent the spatial resolution in its transaxial and axial components. In this paper, we are interested in understanding the spatial resolution limitation projected in any given one of these directions (designated below by an '*x*') for a point source. We will refer to this physical quantity as the 'spatial resolution". There are several independent components that contribute to the overall point source spatial resolution attained in PET systems. We assume these blurring factors are each isotropic in the transaxial and axial directions:

(a) *Detector size*. Since there is no information on where within a detector element a given annihilation photon enters, the detector width in any given direction plays an important role in the measured spatial resolution. Since theoretically the detector sensitivity to coincident lines of response in any given direction x is maximum at the detector centre and falls off to zero at the edge, this factor $D(x)$ is modelled as a triangular response function (Hoffman *et al* 1982) with its full-width at half-maximum (FWHM) equal to one-half the detector element width: $D(x) = w/2$, where w is the detector width in either the transaxial or axial directions. It is noted that in order to obtain this ideal triangular shape, it is assumed that the point source is near the centre of the scanner and the detector width w is much smaller than the system diameter (Hoffman *et al* 1982).

(b) *Annihilation photon non-collinearity*. Because the centre of mass of the positron and atomic electron system is not always at rest at their annihilation, in order to conserve energy and

momentum, the annihilation photons created are not always 180° apart. The linear fluctuation of this contribution in any given direction x is a 1D projection of a 2D blurring function, and is modelled as a Gaussian distribution $N(x)$ centred at the origin: $N(x) = A \, \mathrm{e}^{-x^2/2\sigma^2}$, where FWHM $= 2.35\sigma = 0.0022d_s$ (in mm), with d_s the system diameter (in mm) (DeBenedetti *et al* 1950, Moses and Derenzo 1993). The corresponding angular fluctuation is: $\Delta\phi = 0.0044$ rad FWHM).

(c) *Positron range.* $P(x)$, the positron annihilation point spread function (or positron range blurring function) in any given direction x was found to be 'cusp-like' as calculated by the Monte Carlo beta trajectory simulation. This spherically symmetric point spread function was calculated in three dimensions and $P(x)$ is the 1D histogram of this distribution. The histogram bin size used is much smaller than the detector size since theoretically the true positron blurring function is independent of detector size (the distribution exists independent of the measurement parameters). We studied the shape of the positron range blurring function in one direction (transaxial, for example) as a function of the dimension of acceptance in the other direction (axial, for example). The resulting functions were all cusp-like with similar shapes, but different areas under the curves. Thus, in the spatial resolution calculation, we will assume the shape of the normalized positron range blurring function in one dimension (transaxial, for example) is independent of the measurement parameters in the other dimension (axial, for example).

(d) *Detector effects.* Intercrystal Compton scatter of annihilation photons (Levin *et al* 1997) and scintillation light multiplexing (Moses and Derenzo 1993) can be sources of positioning errors. These effects can be compensated for in detector design (Moses and Derenzo 1994).

(e) *Depth of interaction.* Detector penetration by annihilation photons originating away from the PET scanner axis can lead to incorrect line of response assignment. Fortunately, this effect can also be compensated for in detector design (Moses and Derenzo 1994, Casey *et al* 1997).

(f) *Source size and motion.* We will assume a static point source of positron activity.

Thus, it appears that the unavoidable physical limitations of PET system spatial resolution are due to *detector element size, photon non-collinearity* and *positron range*. The positron range effect depends on the isotope but is constant for all systems; the other two depend on system parameters, but have the same contributions to the resolution blurring for all isotopes. The overall PET system spatial resolution function for a point source, $R(x)$, is an integral convolution of the three main physical blurring functions $P(x)$, $N(x)$ and $D(x)$:

$$R = P \otimes N \otimes D \tag{15}$$

or

$$R(x) = \int_{-\infty}^{\infty} P(y) \int_{-\infty}^{\infty} N(z) D(x - y - z) \, \mathrm{d}z \, \mathrm{d}y.$$

The calculation of $R(x)$ is performed for each of the four isotopes of interest. The three distributions (P, N and D) are normalized and have identical bin widths of 10 μm.

3. Results

3.1. Experimental validation

The results from the beta transmission/absorption measurements were compared with those from the corresponding simulations. Both the measured energy spectra, the data for electron
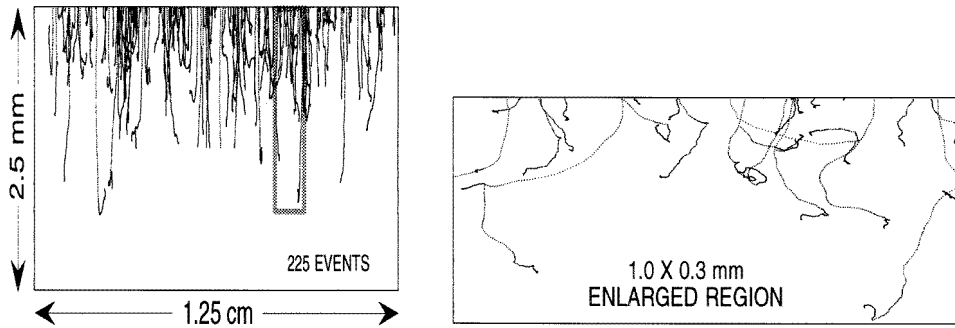
Figure 3. Left: simulated electron trajectories in a plastic absorber from a [204]Tl flood source. Note the expanded *y*-axis. Right: enlarged view within the grey rectangle in the left plot with correct *x*–*y* proportions.
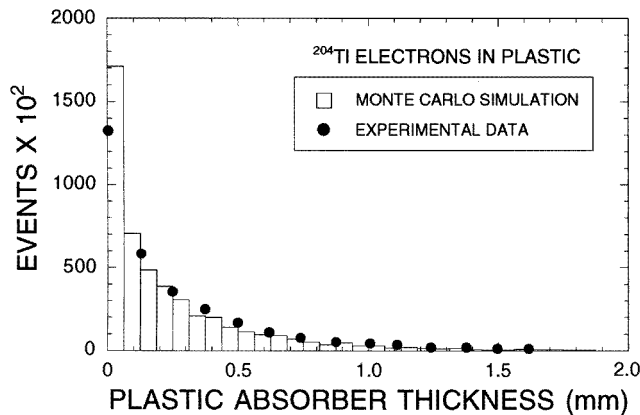
Figure 4. Distribution of [204]Tl beta ranges (maximum spatial extent in 1D) in plastic as a function of plastic absorber thickness as calculated by the Monte Carlo simulation and as measured using beta absorption/transmission studies.

beam attenuation with increasing thickness, and the overall maximum extent of the [204]Tl betas (∼1.7 mm) corresponded well with that calculated from the electron trajectory Monte Carlo. Figures 3–5 show these results. Figure 3 shows a two-dimensional projection of 225 simulated electron trajectories within a 2.5 mm thick, 1.25 cm wide slab of the plastic absorber from a [204]Tl flood source. An enlargement of the data within the grey rectangle is shown on the right. It is clear from these plots that scatter at small angles is dominant along the beginning of the track. At higher energy the scattering involves primarily small-angle deflections. The multiple scatter angle is inversely related to the beta energy, and where the energy is lowest, the scatter angle is highest. dE/dx also rapidly increases as the electron slows down. Thus, towards the end of the trajectory scattering at large angles becomes more frequent, and the electron's path begins to show more curvature (figure 3, right).

Figure 4 shows a histogram of the distribution of the beta maximum spatial extent ('range') for 400 000 [204]Tl beta events calculated by the Monte Carlo superimposed on a plot of the measured beta particle transmission as a function of absorber thickness (the two distributions
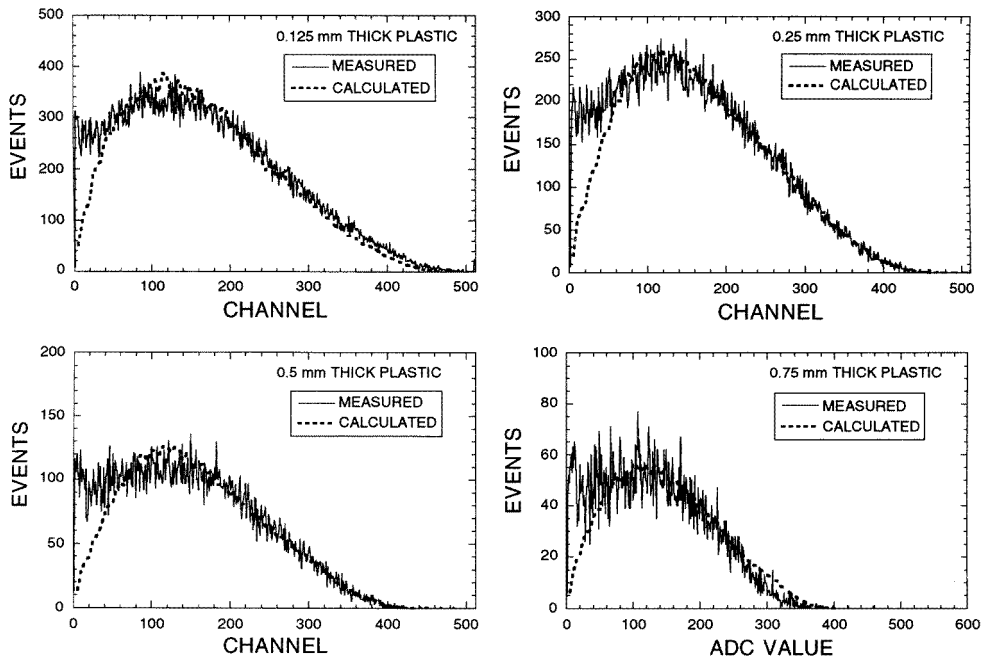
Figure 5. Comparison between the calculated and measured energy spectra of transmitted [204]Tl beta particles for four plastic absorber thicknesses.

are normalized to the same value). There is good agreement between the calculated and the measured distributions for all absorber thicknesses studied, indicating that the physics is adequately modelled in the simulation. In particular, the calculated maximum spatial extent for all [204]Tl betas is roughly 1.7 mm, and, indeed, a 1.7 mm thick slab of plastic absorber was required to prevent any measured beta transmission to the detector.

Figure 5 shows the calculated beta transmission energy spectra for four different absorber thicknesses plotted on top of the corresponding measured data (with background subtraction). The calculation is consistent with the measurement down to roughly 50 keV. This discrepancy may be due to (a) additional low-energy, x-ray background emissions from source effects that were underestimated before their subtraction from the measured spectra, or (b) the breakdown of the multiple scattering formulation for low-energy absorption as discussed in section 2.1.1. The fewer lower-energy events derived from the calculation compared to the measurements for energies less than roughly 50 keV means that the number of events that travel less than ∼0.1 mm will be slightly underestimated by the calculation.

3.2. Simulated positron trajectories

Figure 6 shows a two-dimensional projection of 100 simulated positron trajectories for an ^{18}F point source in water. Near the end of any given positron track, large-angle scatter occurs continuously within a small region with the result that the positron winds around quite abruptly as it slows to a stop and a significant fraction of the total energy of that event is deposited near the end of its track. Note the creation of delta electrons ejected at large angles to the track of a few of the positron trajectories shown.
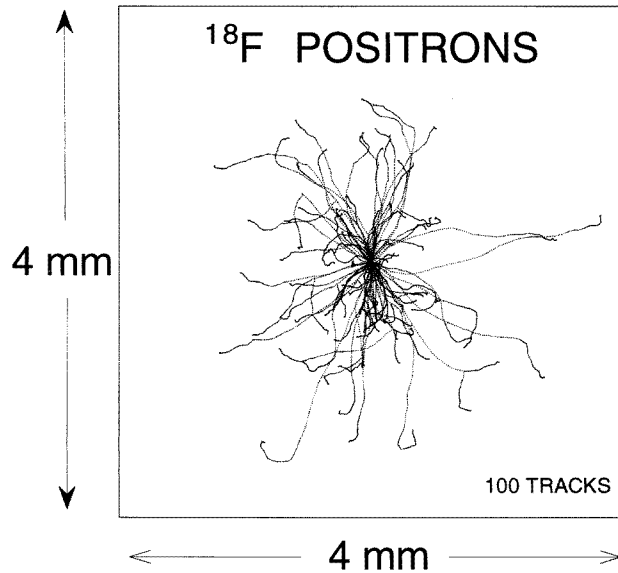
Figure 6. Simulated ^{18}F positron tracks from a point source in water.

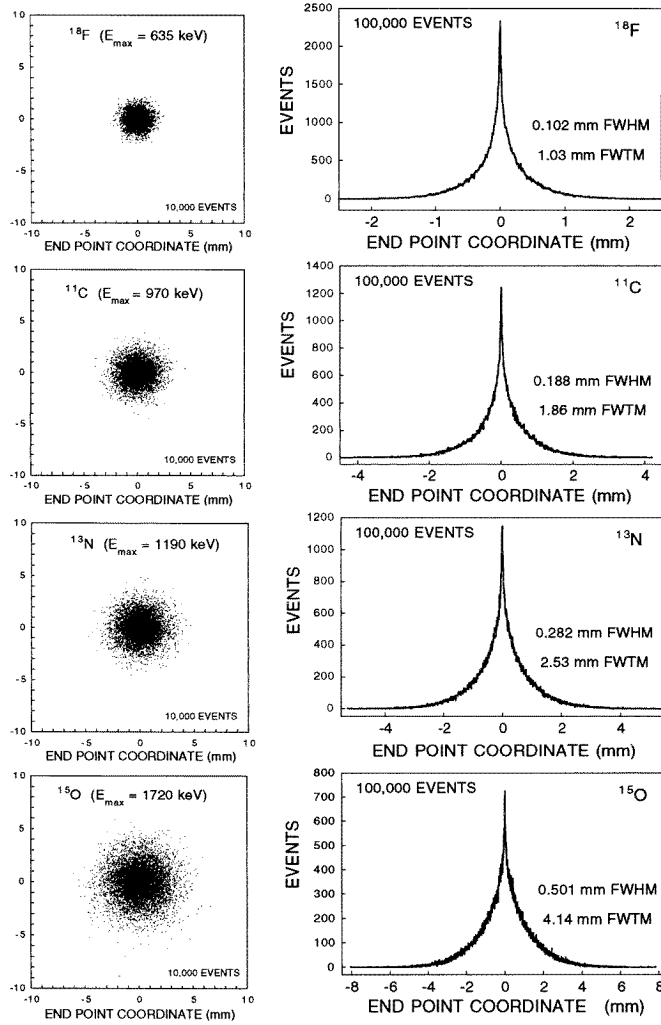### 3.3. Positron annihilation point distribution

The end point is where the positron annihilates with an atomic electron and creates the two 511 keV photons. The distribution of the end points determines the contribution of the spatial extent of the positron trajectory to the spatial resolution of a PET system. This section presents the results of these calculations for ^{18}F, ^{11}C, ^{13}N and ^{15}O in water.

Figure 7 (left) shows a two-dimensional scatter plot distribution of the ^{18}F, ^{11}C, ^{13}N and ^{15}O positron end point coordinates for 10 000 trajectories originating from a point location. To the right of each figure is a one-dimensional histogram of the x-coordinates of the three-dimensional distribution, which is relevant to the image spatial resolution in any given direction. Due to the fact that a significant fraction of the events travel less than 0.5 mm as discussed in section 2.1.2, the resulting shape of the positron end point coordinate distribution is 'cusp-like' in shape. The data shown in figure 7 are presented with 100 bins/mm or 10 μm bins, which we considered to be adequate and appropriate sampling. The FWHM and FWTM give a conventional measure of resolution blurring due to any given factor. We note, however, in the case of a cusp-like function, that these parameters are somewhat dependent on the bin or sample size and do not have a strict meaning (although below $\sim$15 μm bin size, this dependence is not strong). The FWHM and FWTM values of the distribution are shown on the respective figures. We note that the positive side of the cusp-like distributions could be fitted well to the sum of two exponential functions (Derenzo 1979) of the form

$$P(x) = C\,\mathrm{e}^{-k_1 x} + (1 - C)\,\mathrm{e}^{-k_2 x} \qquad x \geqslant 0 \tag{16}$$

with the parameters C, k_1 and k_2 for the best fit given in table 1 for the four isotopes.

The central spike in each of the resulting distributions of figure 7 preserves some of the high spatial frequency information of the signal (for better spatial resolution), although more so for ^{18}F than for ^{15}O. In figure 8 we plot the modulation transfer function (MTF) for the four distributions (positive frequency components only). We see that, as expected, the end point distributions for the lower-energy sources contain a larger proportion of higher
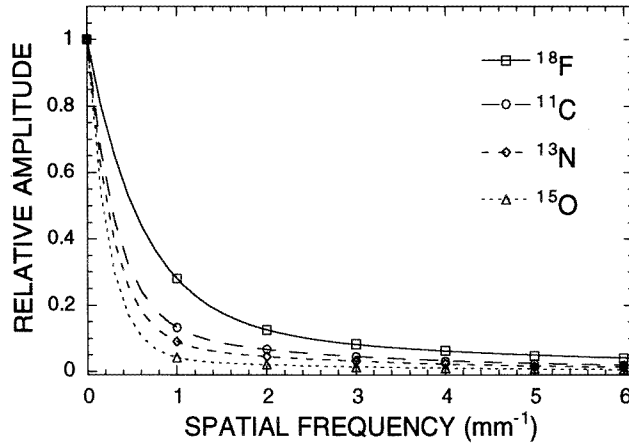
Figure 7. Left: calculated distribution of positron annihilation coordinates in water projected onto a plane for ^{18}F, ^{11}C, ^{13}N and ^{15}O sources. Right: histogram of x coordinates from positron annihilation point distribution.

Table 1. Best fit parameters of equation (16) to the 1D distributions ($x \geqslant 0$) shown in figure 7.

	^{18}F	^{11}C	^{13}N	^{15}O
C	0.516	0.488	0.426	0.379
k_1 (mm^{-1})	0.379	0.238	0.202	0.181
k_2 (mm^{-1})	0.031	0.018	0.014	0.009

spatial frequency components. However, low frequencies dominate the spectrum. For all distributions, roughly 70% of the signal is preserved within a cut-off frequency of 20 mm^{-1}. Thus, when studying positron range effects on spatial resolution, FWTM should be considered along with the FWHM values, especially for the higher endpoint energy positron sources.

Figure 8. Modulation transfer function (MTF) (positive frequencies only) for the calculated ^{18}F, ^{11}C, ^{13}N and ^{15}O 1D annihilation point distributions of figure 7.
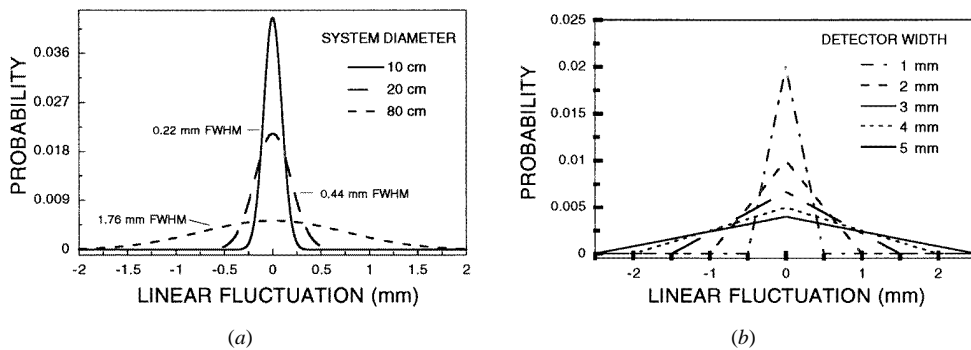

Figure 9. Calculated blurring functions due to (*a*) positron annihilation photon non-collinearity for 10, 20 and 80 cm diameter systems, and (*b*) finite detector element size for 1–5 mm widths.

3.4. Detector size and annihilation photon non-collinearity point spread functions

Figures 9(*a*) and (*b*), respectively, show the annihilation photon non-collinearity and detector size response distributions for system diameters of 10, 20 and 80 cm, and detector element (crystal) widths of 1, 2, 3, 4 and 5 cm. Large system diameters and coarse detector elements will add significant blurring to the total system spatial resolution.

3.5. PET system spatial resolution components

Figures 10 and 11 give examples of the calculated spatial resolution components and their convolution for ^{18}F and ^{15}O, the lowest and highest energy (and range) positron sources studied. Figure 10(*a*) shows ^{18}F results for a 2 mm diameter detector width and 20 cm system diameter and figure 10(*b*) shows the case for a 4 mm detector width and 80 cm diameter. The combined system spatial resolutions are 1.4 mm FWHM (2.7 mm FWTM), for the former system parameters and 2.9 mm FWHM (5.2 mm FWTM) for the latter. For the smaller detector and scanner diameter sizes, the ^{18}F positron range and detector size effects dominate, while for the large detector and scanner case, the non-collinearity and detector size dominate.
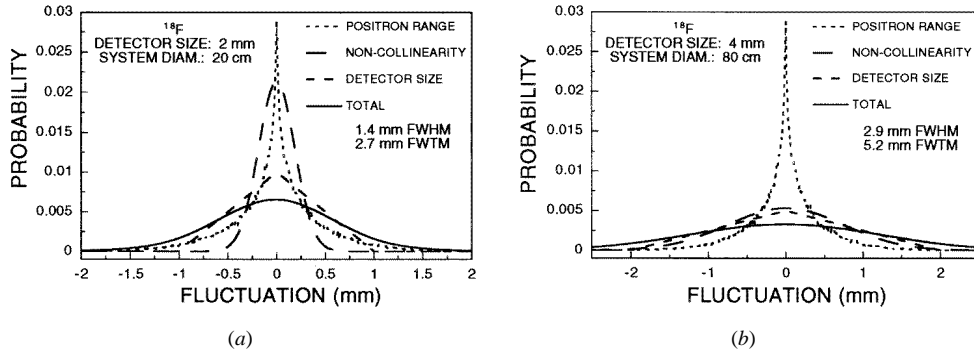
Figure 10. Calculated spatial resolution blurring factors and their combination for ^{18}F with (*a*) 20 cm system diameter and 2 mm wide detectors, and (*b*) 80 cm system diameter with 4 mm detectors.
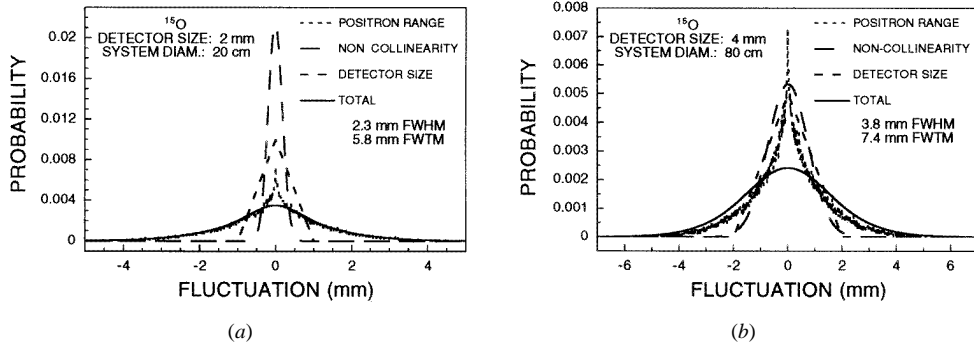
Figure 11. Calculated spatial resolution blurring factors and their combination for ^{15}O with (*a*) 20 cm diameter system and 2 mm wide detectors, and (*b*) 80 cm system diameter with 4 mm wide detectors.

Figures 11(*a*) and (*b*) show ^{15}O functions for the same two configurations of detector and scanner dimensions. The resolution results for ^{15}O are 2.3 mm FWHM (5.8 mm FWTM) for the first case and 3.8 mm FWHM (7.4 mm FWTM) for the second. For the small detector and scanner dimensions, the ^{15}O positron range clearly dominates, while for the second case, all three components are important.

3.6. PET system design and spatial resolution

In figure 12, we plot the combined system spatial resolution as a function of detector element width for ^{18}F, ^{11}C, ^{13}N and ^{15}O studies. Because the fundamental physical limits on PET system spatial resolution are determined by positron range, photon non-collinearity and detector element size effects, simply reducing the detector element size may not significantly improve combined system resolution for all configurations.

4. Discussion and conclusion

We have developed a Monte Carlo simulation (figure 2) that calculates positron (or electron) trajectories in dense media and validated the calculation with a comparison with beta
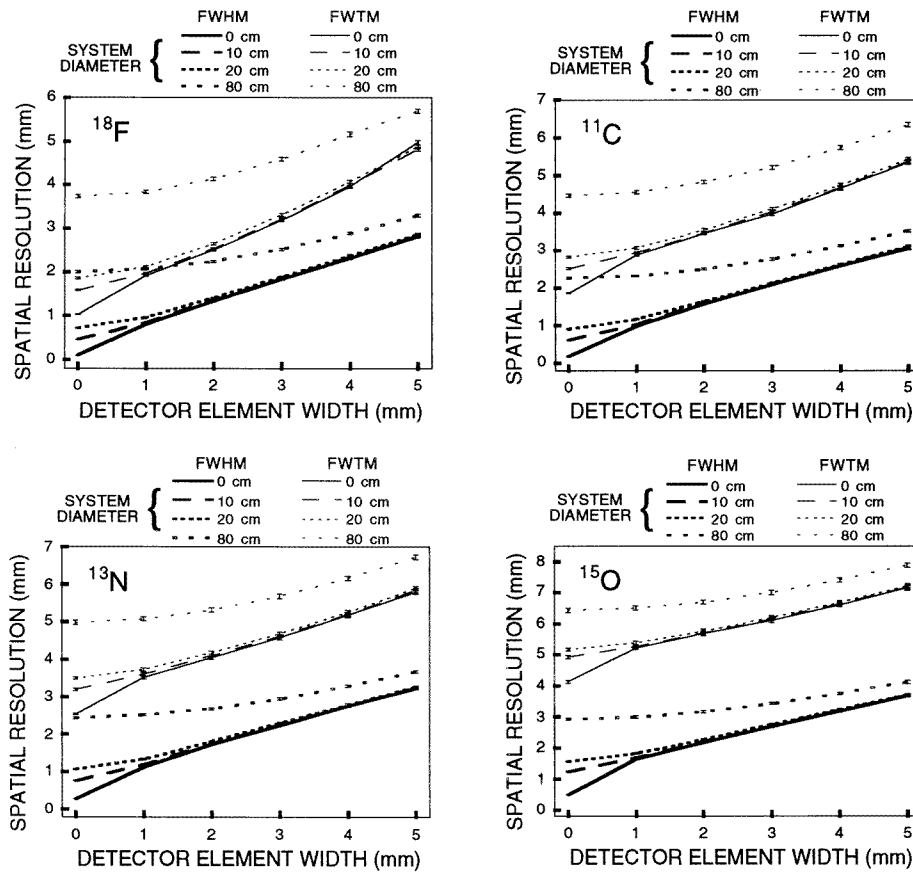
Figure 12. Calculated fundamental system spatial resolution limits at FWHM and FWTM as a function of detector element width for system diameters of 0, 10, 20 and 80 cm using ^{18}F, ^{11}C, ^{13}N and ^{15}O sources.

transmission and absorption measurements (figures 3–5). For the energies of interest, beta trajectories initially show only small deviations from the original direction, but as the particle slows down, larger-angle scattering and energy loss causes the particle's path to wind around. The result is that a large fraction of the beta energy is deposited near the end of its track (figure 3).

The 'unavoidable' physical limits of spatial resolution in PET are due mainly to positron range, annihilation photon non-collinearity and detector element width. Positron annihilation point distributions calculated from the simulation for ^{18}F, ^{11}C, ^{13}N and ^{15}O point sources in water are 'cusp-like' in shape (figures 6 and 7). The positron range blurring function for ^{15}O is over a factor of four wider at FWHM and FWTM than for ^{18}F due to the nearly three times greater average positron emission kinetic energy (figures 1 and 7). The cusp-like shape tends to preserve some of the high spatial frequency information (figures 7 and 8). However, the long tails (low-frequency portion) of the distributions limit the spatial resolution attainable, especially at FWTM (figures 7, 10, 11 and 12), causing the corresponding image to be blurred severely. Thus, when considering positron range effects on spatial resolution, both FWHM and FWTM are important. Fluctuations due to photon non-collinearity and detector size are

nearly Gaussian and triangular in shape, respectively, and can cause significant blurring as a function of system diameter and detector element width (figures 9, 10, 11 and 12).

A comparison with the positron annihilation point distribution results of Derenzo (1979) is difficult to make. The bin size used was 10 μm in our calculated distribution in water and $\geqslant$5 mm in Derenzo's (1979) measurements in polyurethane foam, and values of the FWHM and FWTM are sensitive to the bin width for cusp-like functions. In addition, our calculation was performed for an ideal point source, while the exact shape of the source described in Derenzo's (1979) paper was probably more disc-like. However, if we force a comparison we note that our ^{18}F calculated point source value of 0.10 mm FWHM for the positron range blurring function compares reasonably well with Derenzo's point spread function value of 0.13 mm deconvolved and extrapolated from measurements in polyurethane foam (Derenzo 1986; see table 1). The calculated FWTM value of 1.0 mm, however, does not correspond well with the Derenzo value of 0.38 mm. Our calculated ^{11}C values of 0.19 mm FWHM and 1.9 mm FWTM also do not compare well with the corresponding values of 0.13 and 0.39 mm obtained by Derenzo (1986, table 1). ^{18}F and ^{11}C positron sources have significantly different energy distributions (see figure 1; E_{max} (^{18}F) = 635 keV, E_{mean} (^{18}F) = 250 keV, E_{max} (^{11}C) = 970 keV, E_{mean} (^{11}C) = 390 keV). Thus, it seems unlikely that these two isotopes could have essentially the same FWHM and FWTM annihilation point distribution values.

We have calculated the overall system spatial resolution by convolving the three basic fluctuation components with the following results relevant to scanner design for ^{18}F, ^{11}C, ^{13}N and ^{15}O isotopes (see figures 10–12):

(a) ^{18}F. For $\leqslant$ 20 cm diameter scanners (typical for animal imaging system designs), the FWHM and FWTM spatial resolution improves with smaller crystals, but there is no significant resolution difference between scanner diameters until the crystal size is <1 mm. Decreasing the detector element width below 1 mm will improve the system spatial resolution with the fundamental limit of ~0.6 mm FWHM (1.8 mm FWTM) for an infinitely thin detector. For an 80 cm diameter system the resolution improvement saturates below 2 mm crystal width (at ~2.0 mm FWHM, 3.7 mm FWTM) since the response is dominated by photon non-collinearity. All scanner diameters show improved FWTM spatial resolution with smaller crystals since the positron range effect for ^{18}F is a relatively small factor. Note that for crystal size <1 mm the 80 cm diameter FWHM resolution values are actually worse than the FWTM values for smaller system diameters.

The ^{18}F combined system response function examples shown in figure 10, with 2 mm detector width, 20 cm system diameter and 4 mm detector width, 80 cm diameter, correspond roughly to the UCLA μPET (Chatziioannou *et al* 1997) and the CTI (Knoxville, TN) HR+ tomograph designs respectively. The calculated ^{18}F point source resolution values reported here for the first configuration are 1.4 mm FWHM and 2.7 mm FWTM in-plane. The corresponding measured results reported from the UCLA μPET group are 1.5 mm FWHM and 2.7 mm FWTM at the centre (Chatziioannou *et al* 1997), which compare well with the calculated values. The calculated ^{18}F resolution values for the second case are 2.9 mm FWHM and 5.2 mm FWTM in-plane. The corresponding reported values measured with the CTI HR+ scanner (Adam *et al* 1997) of 4.5 mm FWHM and 8.1 mm FWTM do not compare well with the calculated values. We believe the main reason that the μPET results compared well with the calculation and the HR+ results do not is due to the fact that the signal in the former design at the centre of the tomograph is adequately sampled (Chatziioannou *et al* 1997) and is not in the latter. The inadequate sampling inherent in the HR+ is expected to add of the order of 25% to the reconstructed resolution (Moses and Derenzo 1993). An extra blurring effect that is thought to be present in the HR+ design and not in the μPET design is the so-called 'block factor'

(Moses and Derenzo 1993, Adam *et al* 1997) due to the inherent light multiplexing in the PET block detector design. This hypothetical factor is expected to add a Gaussian contribution of roughly 2 mm FWHM (3.7 mm FWTM). With this new factor added in quadrature to the calculated value and the undersampling factor of 1.25 taken into account, the modified calculated resolution values are roughly 4.4 mm FWHM and 8.0 mm FWTM, which compare well with the measured values.

(b) ^{11}C. Similar conclusions for ^{18}F are also true for ^{11}C except the system resolution values are worse and the FWTM values do not improve as drastically with narrower crystal widths due to the larger positron range blurring effect. The fundamental spatial resolution limit for infinitely thin detectors is ~0.9 mm FWHM (2.8 mm FWTM) for animal systems ($\leqslant$20 cm diameter), and ~2.3 mm FWHM (4.5 mm FWTM) for human scanners (80 cm diameter).

(c) ^{13}N. The same basic conclusions also hold except, due to a larger positron range blurring effect, the FWHM resolution values are even higher and the FWTM values are less affected by crystal size. The latter result is also true for the 80 cm system at FWHM using ^{13}N. The fundamental spatial resolution limit for infinitely thin detectors is ~1.0 mm FWHM (3.5 mm FWTM) for animal systems ($\leqslant$20 cm diameter), and ~2.5 mm FWHM (5.0 mm FWTM) for human scanners (80 cm diameter).

(d) ^{15}O. Same as for ^{13}N, except with even worse resolution values. Note that for higher-energy isotopes the difference between the FWHM and FWTM values increases for all system design configurations, and the 80 cm diameter resolution values are less affected by crystal size due to the dominance of positron range effects. For human imaging system design (~80 cm diameter), if significant ^{15}O imaging is expected, then a detector element width of 3–4 mm will allow nearly optimal spatial resolution of roughly 3.0 mm FWHM (6.5 mm FWTM). For animal PET systems ($\leqslant$20 cm diameter), smaller detector elements improve spatial resolution with the fundamental spatial resolution limit of ~1.6 mm FWHM (5.2 mm FWTM) (compare with 0.6 mm FWHM (1.8 mm FWTM) for ^{18}F).

Finally it should be noted that using smaller detector elements in PET system design with the goal of improving system spatial resolution may not always be advisable. Sensitivity issues are equally important and the required signal-to-noise ratio per image pixel should be considered as well.

Acknowledgments

References

Adam L, Zaers J, Ostertag H, Trojan H, Bellemann M E and Brix G 1997 Performance evaluation of the whole-body PET scanner ECAT EXACT HR+ following the IEC standard *IEEE Trans. Nucl. Sci.* **44** 1172–9
Bethe H 1953 Moliere's theory of multiple scattering *Phys. Rev.* **89** 1256–66
Casey M E, Eriksson L, Schmand M, Andreaco M S, Paulus M J, Dahlbom M and Nutt R 1997 Investigation of LSO crystals for high spatial resolution positron emission tomography *IEEE Trans. Nucl. Sci.* **44** 1109–13
Chatziioannou A, Cherry S R, Shao Y, Silverman R W, Meadors K, Farquhar T and Phelps M E 1997 MicroPET I: performance evaluation of a very high resolution PET scanner for imaging small animals *J. Nucl. Med.* **38** 7
Cherry S R, Shao Y, Siegel S, Silverman R W, Mumcuoglu E, Meadors K and Phelps M E 1996 Optical fiber readout of scintillator arrays using a multi-channel PMT: a high resolution PET detector for animal imaging *IEEE Trans. Nucl. Sci.* **43** 1932–7

Cho Z H, Chan J K, Ericksson L, Singh M, Graham S, MacDonald N S and Yano Y 1975 Positron ranges from biomedically important positron-emitting radionuclides *J. Nucl. Med.* **16** 1174–6

Daniel H 1968 Shapes of beta-ray spectra *Rev. Mod. Phys.* **40** 659–72

DeBenedetti S, Cowan C E, Konneker W R and Primakoff H 1950 On the angular distribution of two-photon annihilation radiation *Phys. Rev.* **77** 205–12

Derenzo S E 1979 Precision measurement of annihilation point spread distributions for medically important positron emitters *Positron Annihilation* ed R R Hasiguti and K Fujiwara (Sendai, Japan: The Japan Institute of Metals) pp 819–23

——1986 Mathematical removal of positron range blurring in high resolution tomography *IEEE Trans. Nucl. Sci.* **33** 565–9

Hoffman E J, Huang S C, Plummer D and Phelps M E 1982 Quantitation in positron emission computed tomography: 6. Effect of nonuniform resolution *J. Comput. Assist. Tomogr.* **6** 987–99

Hoffman E J, Phelps M E, Mullani N A, Higgins S C and Ter-Pogossian M M 1976 Design and performance characteristics of a whole-body positron transaxial tomograph *J. Nucl. Med.* **17** 493–502

Iida H, Kanno I, Miura S, Murakami M, Takahashi K and Uemura K 1986 A simulation study of a method to reduce positron annihilation spread distributions using a strong magnetic field in positron emission tomography. *IEEE Trans. Nucl. Sci.* **33** 597–600

Katz L and Penfold A S 1952 Range-energy relations for electrons and the determination of beta-ray end-point energies by absorption *Rev. Mod. Phys.* **24** 28–44

Knoll G F 1989 *Radiation Detection and Measurement* (New York: Wiley) ch 2

Leo W R 1987 *Techniques for Nuclear and Particle Physics Experiments* (New York: Springer) ch 2

Levin C S, Hoffman, E J and Cherry S R 1997 Positron range calculation and its effect on positron emission tomography spatial resolution *IEEE Medical Imaging Conf. (Albuquerque, NM, 1997)* (Poster)

Levin C S, MacDonald L R, Tornai M P, Hoffman E J and Park J 1996 Optimizing light collection from thin scintillators used in a beta-ray camera for surgical use *IEEE Trans. Nucl. Sci.* **43** 2053–60

Levin C S, Tornai M P, Cherry S R, MacDonald L R and Hoffman E J 1997 Compton scatter and x-ray crosstalk and the use of very thin intercrystal septa in high resolution PET detectors *IEEE Trans. Nucl. Sci.* **44** 218–24

Moses W W and Derenzo S E 1993 Empirical observation of resolution degradation in positron emission tomographs utilizing block detectors *J. Nucl. Med.* **34** 101

——1994 Design studies for a PET detector module using a PIN photodiode to measure depth of interaction *IEEE Trans. Nucl. Sci.* **41** 1441–5

Palmer M R and Brownell G L 1992 Annihilation density distribution calculations for medically important positron emitters *IEEE Trans. Med. Imaging* **11** 373–8

Phelps M E, Hoffman E J and Huang S 1975 Effects of positron range on spatial resolution *J. Nucl. Med.* **16** 649–52

Raylman R R, Hammer B E and Christensen N L 1996 Combined MRI–PET scanner: a Monte Carlo evaluation of the improvements in PET resolution due to the effects of a static homogeneous magnetic field *IEEE Trans. Nucl. Sci.* **43** 2406–12

Rickey D W, Gordon R and Huda W 1991 On lifting the inherent limitations of positron emission tomography by using magnetic fields (MagPET) *Automedica* **14** 355–69

Ritson D M 1961 *Techniques of High Energy Physics* (New York: Interscience) ch 1

Rohrlich F and Carlson B C 1954 Positron-electron differences in energy loss and multiple scattering *Phys. Rev.* **93** 38–44

Schmelz C, Bradbury S M, Holl I, Lorenz E, Renker D and Ziegler S 1995 Feasibility study of an avalanche photodiode readout for a high resolution PET with nsec time resolution *IEEE Trans. Nucl. Sci.* **42** 1080–4

Seidel J, Gandler W R and Green M V 1994 A very high resolution single slice small animal PET scanner based on direct detection of coincidence line endpoints *J. Nucl. Med.* **35** 40P (abstract)

Siegbahn K 1955 *Beta- and Gamma-ray Spectroscopy* (New York: Interscience) ch 1

Watanabe M, Omura T, Kyushima H, Hasegawa Y and Yamashita T 1995 A compact position-sensitive detector for PET *IEEE Trans. Nucl. Sci.* **42** 1090–4

Weber S, Terstegge H, Halling H, Herzog H, Reinartz R, Reinhart P, Rongen F and Muller-Gartner H W 1995 The design of an animal PET: flexible geometry for achieving optimal spatial resolution or high sensitivity *Conf. Record IEEE Medical Imaging Conf. (San Francisco, CA)* #95CH35898 (Piscataway, NJ: IEEE) pp 1002–5

Wirrwar A, Vosberg H, Herzog H, Halling H, Weber S and Muller-Gartner H W 1997 4.5 Tesla magnetic field reduces range of high-energy positrons—potential implications for positron emission tomography *IEEE Trans. Nucl. Sci.* **44** 184–9

Wu C S and Moskowski S A 1966 *Beta Decay* (New York: Interscience)